Available online at www.sciencedirect.com
SCIENCE DIRECT®
Experimental Thermal and Fluid Science 30 (2005) 37–47
Experimental Thermal and Fluid Science
www.elsevier.com/locate/etfs

Air–water and momentum exchanges in unsteady surging waters: An experimental study

Hubert Chanson *

Department of Civil Engineering, The University of Queensland, Brisbane QLD 4072, Australia

Received 7 July 2004; accepted 3 March 2005

Abstract

Flood waves resulting from dam breaks and flash floods have been responsible for numerous losses. In the present study, sudden flood releases were investigated down a large flume with a succession of abrupt drops. A new experimental technique was developed to obtain instantaneous void fractions, bubble count rates and velocities using arrays of conductivity probes. The results showed the surge propagating as a succession of free-jets and horizontal runoff flow motion downstream of each abrupt drop. A strong aeration of the surge leading edge was observed for all investigated flow conditions. In the horizontal runoff region, instantaneous velocity measurements highlighted an unsteady turbulent boundary layer. Practically, the study provides new information on free-surface aeration in surging waters in channels and on beach slopes.

Keywords: Surging waters; Air–water measurements; Momentum exchange; Unsteady flow; Shock; Abrupt drop

1. Introduction

Flood waves resulting from dam breaks have been responsible for numerous losses of life. For example, the St Francis dam collapse on the evening of the 12 March 1928 yielded a peak discharge just below the dam of 14,200 m^3/s and 450 people were killed by the flood wave. On 2 December 1959, the Malpasset dam break created a 40 m high wave at 340 m downstream of the dam site and the wave height was still about 7 m about 9 km downstream. More than 300 people died in the catastrophe. Lesser dramatic accidents also caused extensive damage. Bornschein and Pohl [2] documented a dam break which induced major damage when the waters surged through the streets of Glashütte township, Germany. Related situations include flash floods, debris flow surges, glacier lake outburst floods, surging waves in the swash zone, rising tides on dry estuaries and tsunami runup on dry land. In all cases, the surge front is a shock characterised by a sudden discontinuity and extremely rapid variations of flow depth and velocity. Despite few early studies [14,15], current knowledge of dam break wave surging down rough surfaces is rudimentary and the aerated nature of the advancing surge front remains un-quantified, although clearly evidenced by photographs, movies and witness reports (Fig. 1, Table 1).

During the present study, surging waters were investigated in a large-size channel with a rough invert configuration consisting of a succession of abrupt drops. The results provide new information on the surge front propagation. Unsteady two-phase flow measurements were conducted in the surging waters to gain new insights into the air–water flow characteristics and momentum exchanges.

* Tel.: +61 7 33 65 35 16; fax: +61 7 33 65 45 99.
E-mail address: h.chanson@uq.edu.au.

0894-1777/$ - see front matter © 2005 Elsevier Inc. All rights reserved.
doi:10.1016/j.expthermflusci.2005.03.017

Nomenclature

C	void fraction defined as the volume of air per unit volume, also called air concentration
D_t	air bubble diffusivity (m^2/s)
D_0	dimensionless coefficient
d_n	nozzle thickness (m)
d_0	equivalent dam break reservoir depth (m): $d_0 = \frac{9}{4} * \sqrt[3]{\frac{Q(t=0+)^2}{g*W^2}}$
F	bubble count rate (Hz): i.e. number of bubbles detected by the probe sensor per second
f	Darcy–Weisbach friction factor
g	gravity constant (m/s^2) or acceleration of gravity; $g = 9.80$ m/s^2 in Brisbane
h	height of steps (m) (measured vertically)
K'	integration constant
l	horizontal step length (m)
N_{ab}	number of air bubbles detected during the time τ
P	pressure (Pa)
Q	volume flow rate (m^3/s)
$Q(t = 0+)$	volume flow rate (m^3/s) suddenly injected in the channel
q	volume flow rate (m^2/s) per unit width
S_0	average bed slope: $S_0 = \sin\theta$
Tu	turbulence intensity defined as: Tu = u'/V
t	1-time (s); or 2-time (s) from the first water detection by the reference probe
U	free-stream velocity (m/s)
u_r	bubble rise velocity (m/s)
$(u_r)_{Hyd}$	bubble rise velocity (m/s) in hydrostatic pressure gradient
u'	root mean square of longitudinal component of turbulent velocity (m/s)
V	velocity (m/s)
V_s	surge front celerity (m/s)
V_0	characteristic velocity (m/s): $V_0 = Q/(W*d_0)$
W	channel width (m)
x	horizontal distance (m) measured from the abrupt drop
Y_{50}	characteristic depth (m) where $C = 0.50$
Y_{90}	characteristic distance (m) where $C = 0.90$
y	vertical distance (m) measured from the horizontal step face
z	vertical elevation (m)

Greek symbols

ΔX	integration control volume streamwise length (m)
Δx_{tip}	longitudinal distance (m) between probe sensors
δt	interface travel time (s) between probe sensors
μ	water dynamic viscosity (N s/m^2)
ν	water kinematic viscosity (m^2/s)
ν_T	momentum exchange coefficient (m^2/s), also called "eddy viscosity"
θ	angle between the bed slope and the horizontal
ρ	water density (kg/m^3)
τ	integration time (s) for void fraction and bubble count rate calculations

Other symbol

$\varnothing$	diameter (m)

Subscripts

x	horizontal coordinate
y	vertical coordinate

1.1. Bibliography

Hydraulic researchers studied surging flows in laboratory facilities, but the findings are contradictory. For example, some researchers highlighted a boundary layer region in the surge leading edge, including Mano [22] who investigated unsteady wave runup using bubble tracer and high speed video, Fujima and Shuto [16] who performed steady LDA (1 component) measurements on a conveyor belt, and Davies [13] with steady debris flows on a conveyor belt. But Wang [33], based upon video observations, recorded a quasi-linear velocity profile at the head of two-phase debris flow, while Jensen et al. [21] using PIV technique observed a quasi-uniform velocity profile in wave runup on steep beach (also [35]).

Research into highly unsteady gas-liquid flow situations has been very limited with a few exceptions. These include studies of cavitating flows (e.g. [30,31]) and void fraction measurements in breaking waves (e.g. [20,34,18]). Nearly all works were performed on periodic flows enabling repeated measurements.

2. Experimental setup

New experiments were performed in the 24 m long 0.5 m wide flume with a slope $S_0 \approx 0.065$ ($\theta = 3.4°$) previously used by Chanson [9] (Table 1). A precise flow rate was delivered by a pump controlled with an adjustable frequency AC motor drive Taian T-Verter K1/N1 (Pulse Width Modulated design), enabling an accurate discharge adjustment in a closed-circuit system. The flow was fed through a smooth convergent nozzle (1.7 m long), and the nozzle exit was

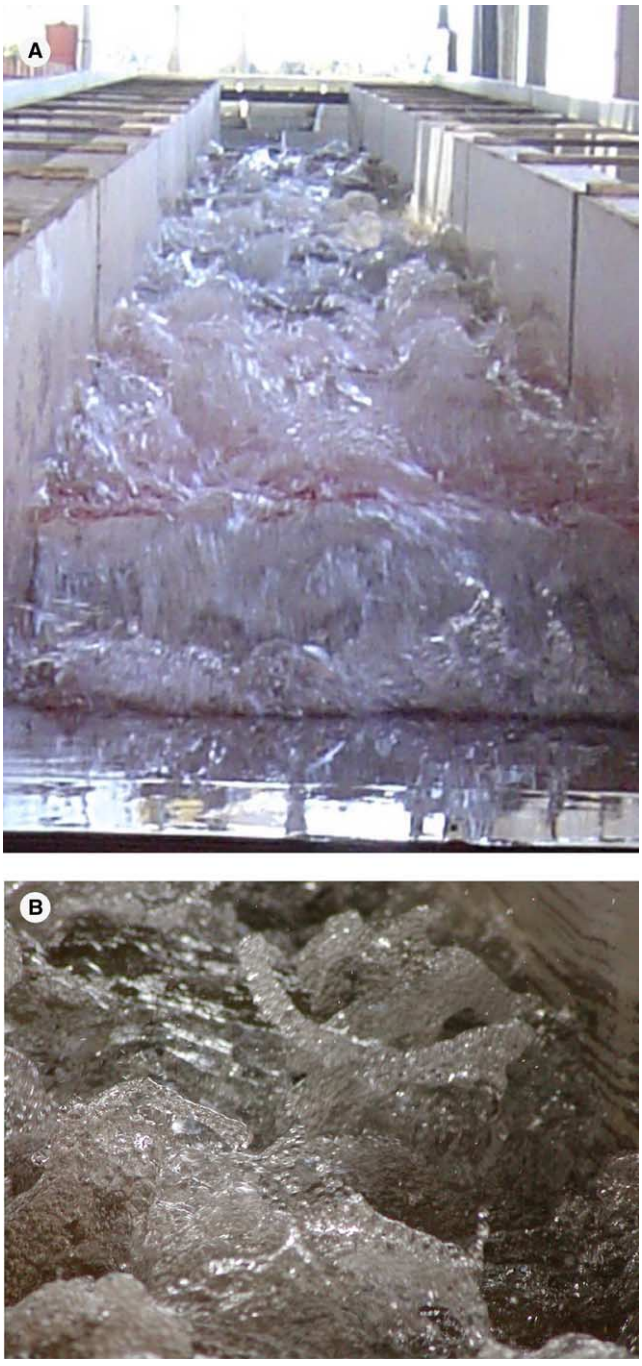

Fig. 1. Advancing flood wave down an initially dry stepped cascade (present study). (A) $Q(t = 0+) = 0.065\ m^3/s$, step 16, $h = 0.0715$ m, $l = 1.2$ m, looking upstream at the advancing surge (Courtesy of Chye-guan SIM, and Chee-chong TAN). (B) Air–water flow structure just behind the flood wave leading edge ($Q(t = 0+) = 0.065\ m^3/s$, step 16, $h = 0.0715$ m, $l = 1.2$ m, looking upstream).

30 mm high and 0.5 m wide. Artificial bed roughness was generated by a stepped invert. The chute consisted of a 2.4 m long horizontal section immediately downstream of the nozzle, followed by 18 identical abrupt drops ($h = 0.0715$ m), each followed by a horizontal step ($l = 1.2$ m).

2.1. Instrumentation

The flow rates in steady flow conditions were measured with a Dall™ tube flowmeter, calibrated on site with a sharp-crested weir. The accuracy on the discharge measurement was about 2%. The surging flow was studied with digital still- and video-cameras using high-shutter speed (1/1000–1/10,000 s) (e.g. Fig. 1B).

Air–water flow properties were measured with two systems. Air concentrations and bubble count rates were recorded with a vertical array of four single-tip conductivity probes (needle probe design). Each probe consisted of a sharpened rod (platinum wire $\varnothing = 0.35$ mm) which was insulated except for its tip and set into a metal supporting tube (stainless steel surgical needle $\varnothing = 1.42$ mm) acting as the second electrode. The second apparatus was a vertical array consisting of a single-tip conductivity probe and a double-tip conductivity probe. For the latter, the inner electrode was a Platinum wire (99.9% purity, $\varnothing = 0.15$ mm) and the outer electrode was a stainless steel surgical needle ($\varnothing = 0.5$ mm). Each tip was identical and the distance between sensor was $\Delta x_{tip} = 8.9$ mm. The probe was designed with a small frontal area of both sensors (i.e. 0.5 mm^2 each) and with a displaced second tip (offset: 1.4 mm) to avoid wake disturbance from the leading tip. With both probe systems, the sensors were aligned along the flow direction and excited by an air bubble detector developed at the University of Queensland (UQ82.518) with a response time of less than 10 μs and calibrated with a square wave generator. The probe output signals were scanned at 10 kHz per channel for 6 s.

Data acquisition was triggered manually immediately prior to the flow arrival to have a minimum of 5 s of record. Visual observations showed that the wave front was roughly two-dimensional. Measurements were conducted on several steps at several distances x from the step vertical face on the chute centreline. At most locations x, a single-tip conductivity probe (i.e. reference probe) was set on the invert, acting as a time reference, while the other probes were set at different elevations (e.g. Fig. 2). In the free-jet region ($x < 0.3$ m), the reference probe was set at the brink height (i.e. $y = h$) to investigate the free-jet flow. Each experiment was repeated until sufficient data were obtained for each vertical profile. The displacement of the probes in the vertical direction was controlled by a fine adjustment travelling mechanism. The error in the probe position was less than 0.2 mm and 2 mm in the vertical and horizontal directions, respectively.

2.2. Data processing

Steps were painted with red and white stripes spaced 50 mm apart. Video-taped movies were analysed

Table 1
Summary of surging open channel flows on initially dry rough channels

Experiment (1)	θ (°) (2)	h (m) (3)	$Q(t = 0+)$ (m^3/s) (4)	Steady flow regime (5)	Remarks (6)
Dressler [14]	0	0.0056	0.0027 0.0076 0.0215	Skimming	65-m long horizontal channel with strip roughness (h = 0.0056 m, l = 0.0224 m). W = 0.225 m
Brushes Clough dam	18.4	0.19	0.5	Skimming	Inclined downward steps, trapezoidal channel (2 m bottom width). 1994 test re-analysed by Chanson [7]
Glashütte dam break	–	–	100–200 (at dam)	–	Failure of 9 m high embankment dam on Tuesday 12 August 2002 [2]
Chanson [9]					25 m long sloping channel
Series 1	3.4	0.143	0.019–0.075	Nappe	10 horizontal steps (l = 2.4 m). W = 0.5 m. Nozzle depth: d_n = 0.030 m
Series 2	3.4	0.0715	0.040–0.075	Transition/skimming	18 horizontal steps (l = 1.2 m). W = 0.5 m. Nozzle depth: d_n = 0.030 m
Present study	3.4	0.0715	0.050 0.060 0.065 0.070	Skimming	18 horizontal steps (l = 1.2 m). W = 0.5 m. Nozzle depth: d_n = 0.030 m

Notes: $Q(t = 0+)$: initial flow rate; d_n: approach flow depth; h: vertical step height (or roughness height); l: horizontal step length (spacing between roughness); W: channel width.

frame-by-frame. The error on the time was less than 1/250 s and the error on the longitudinal position of the wave front was ±1 cm.

The conductivity probe signal outputs were processed using a single threshold technique. The threshold was set at about 50% of air–water voltage range. Unsteady void fractions C and bubble count rates F were calculated during a short time interval τ such as $\tau = \Delta X/V_s$ where V_s is the surge front celerity measured with the video-cameras and ΔX is the control volume streamwise length. Preliminary tests indicated that the control volume length had to satisfy $\Delta X \geqslant 70$ mm to contain a minimum of 5–20 bubbles [8,9]. The selection was consistent with the processing technique of Stutz and Reboud [31] in periodic cavitating flows. The bubble count rate was calculated as: $F = N_{ab}/\tau$ where N_{ab} is the number of bubbles detected during the time interval τ.

Velocity data were calculated from individual droplet/bubble events impacting successively on the two probe sensors. The velocity was deduced from the time lag for air-to-water interface detections by the leading and trailing tips, respectively. For each meaningful event, the interfacial velocity was calculated as: $V = \Delta x_{tip}/\delta t$ where Δx_{tip} is the distance between probe sensors and δt is the interface travelling time between probe sensors.

2.3. Boundary flow conditions

Before each run, the recirculation pipe system and convergent intake were emptied, while the channel was initially dry. The pump was rapidly started and reached nominal discharge $Q(t = 0+)$ in 5 s: that is, at least 10 s prior to the waters entering the channel. The discharge $Q(t = 0+)$ was maintained constant until at least 10 s after the surging waters reached the downstream end of the channel. The steady air–water flow experiments of Chanson and Toombes [10], in the same flume, provided the limiting steady flow conditions of the present study with unsteady flows.

For completeness, preliminary tests were conducted with the channel initially dry and wet. Visual observations demonstrated a major change in wave front shape in presence of an initial film of water. In the presence of an initial layer of fluid, the wave front was led by a positive surge that is a completely different process from surging waters on a dry bed (e.g. [17,23]). Herein, all results corresponded to an initially dry channel bed.

3. Basic observations

For all experiments, visual observations and void fraction data demonstrated that the surging waters propagated as a succession of free-falling nappe, nappe impact and horizontal runoff on each step (Fig. 2). Fig. 2 illustrates a sequence of four instantaneous snapshots of the flow. At each step brink, the advancing surge took off as a free-jet, before impacting onto the downstream step at about $x = 0.2$ to 0.3 m depending upon the flow conditions, where x is the horizontal distance measured from the vertical step face. Nappe impact was associated with very significant spray and splashing, with water droplets reaching heights well in excess of 0.5 m (or 8 step heights). Further, waters started to fill the cavity beneath the nappe, and the cavity became drowned after a period of time. The cavity

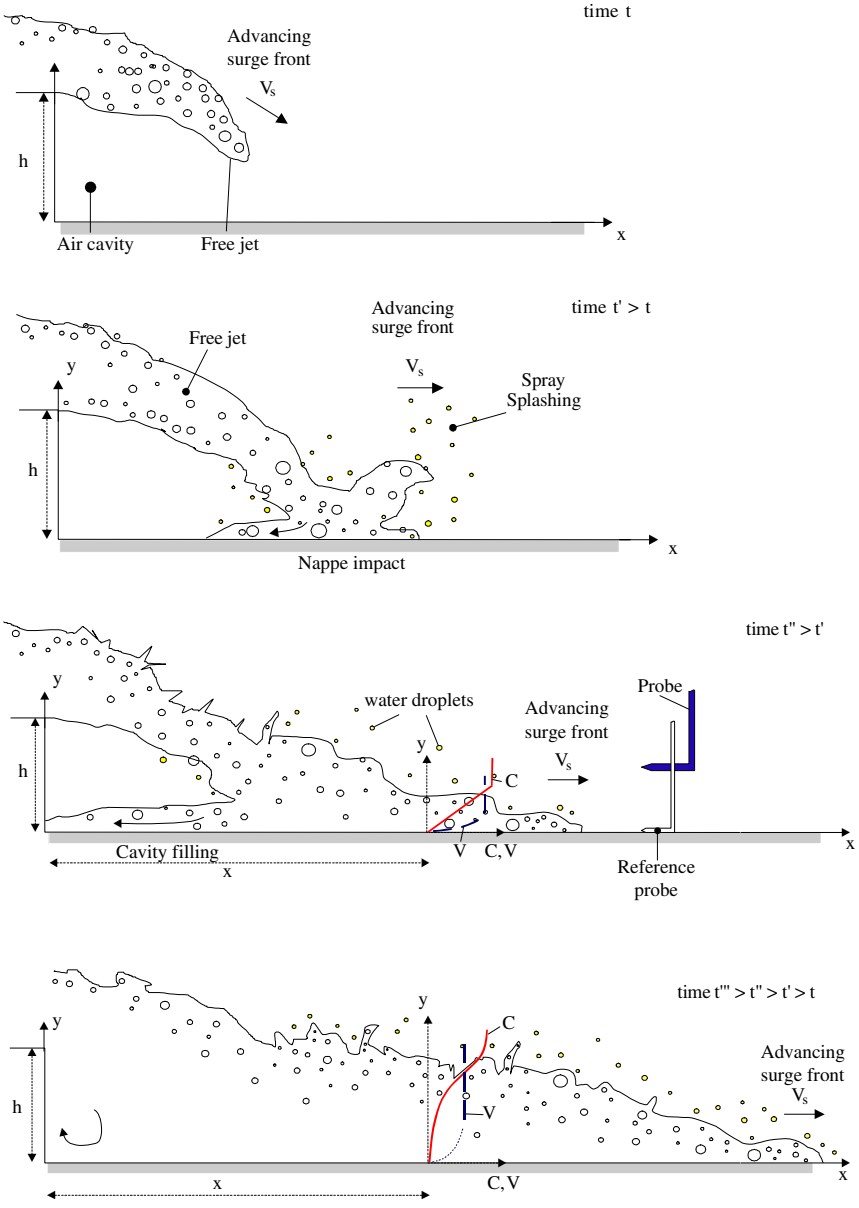

Fig. 2. Definition sketch of advancing surging waters downstream of an abrupt drop.

filling process was however relatively slow compared to the surge propagation on each step. Downstream of nappe impact, the advancing waters ran off the horizontal step as a dam break wave.

In Table 1 (column 5), flow regime observations in steady flows are summarised for comparison. Basically, the surge front exhibited a nappe flow behaviour for all flow conditions in all studies down stepped inclined chutes, although steady flow conditions could correspond to transition or skimming flow regimes as defined by Chanson [7]. Further, the surge leading edge was highly aerated, in particular for the larger flow rates (Fig. 1). Fig. 1A and B emphasise the chaotic nature of the wave front, with strong spray, splashing and wavelets. Water packets were commonly projected to heights greater than 3–5 step heights, while some droplets reached heights of more than 10 step heights. Visually, laboratory experiments in the large-size flume had a similar appearance to prototype surging flows observed during the Glashütte dam break wave surging through the township and during the Brushes Clough dam spillway tests.

The propagation of the surge front was recorded for a range of unsteady flow conditions (Table 1). Wave front celerity data showed some flow acceleration in the first 4–6 steps. Further downstream, a gradual decay in celerity V_s was observed. The data were compared successfully with Hunt [19] theory for dam break wave down sloping chutes. A fair agreement was achieved assuming an equivalent Darcy–Weisbach friction factor

$f = 0.05$, irrespective of flow rate and chute configuration [9, Present study]. This flow resistance value is close to air–water flow measurement results in steady flow conditions yielding $f \sim 0.047$ [10].

4. Void fraction and bubble count rate distributions

Typical measurements of instantaneous void fractions and bubble count rates in the free-jet, at nappe impact and in the horizontal runoff are presented in Figs. 3–5, respectively. In each figure, instantaneous distributions for different times t are shown at a given location x, where t is the time from the first water detection by the reference probe. In Figs. 3–5, the vertical axis is y/d_0 where y is the distance normal to the step invert and d_0 is a measure of the initial flow rate $Q(t = 0+)$:

$$d_0 = \frac{9}{4} * \sqrt[3]{\frac{Q(t=0+)^2}{g * W^2}} \quad (1)$$

g is the gravity acceleration and W is the chute width. In the figures, the legend indicates the location of the control volume relative to the leading edge of shock front: e.g. 0–210 mm means a 210 mm long control volume located between 0 and 210 mm behind the front.

In the free-jet region (i.e. $x < 0.2$–0.3 m), the data showed strong interfacial aeration of both lower and upper nappes. The instantaneous distributions of void fraction followed closely analytical solutions of the air bubble diffusion equations for the upper and lower nappes:

$$C = \frac{1}{2} * \left(1 - \mathrm{erf}\left(\frac{Y_{50} - y}{2 * \sqrt{\frac{D_t}{V_s} * x}}\right)\right) \quad \text{Upper nappe} \quad (2A)$$

$$C = \frac{1}{2} * \left(1 - \mathrm{erf}\left(\frac{y - Y_{50}}{2 * \sqrt{\frac{D_t}{V_s} * x}}\right)\right) \quad \text{Lower nappe} \quad (2B)$$

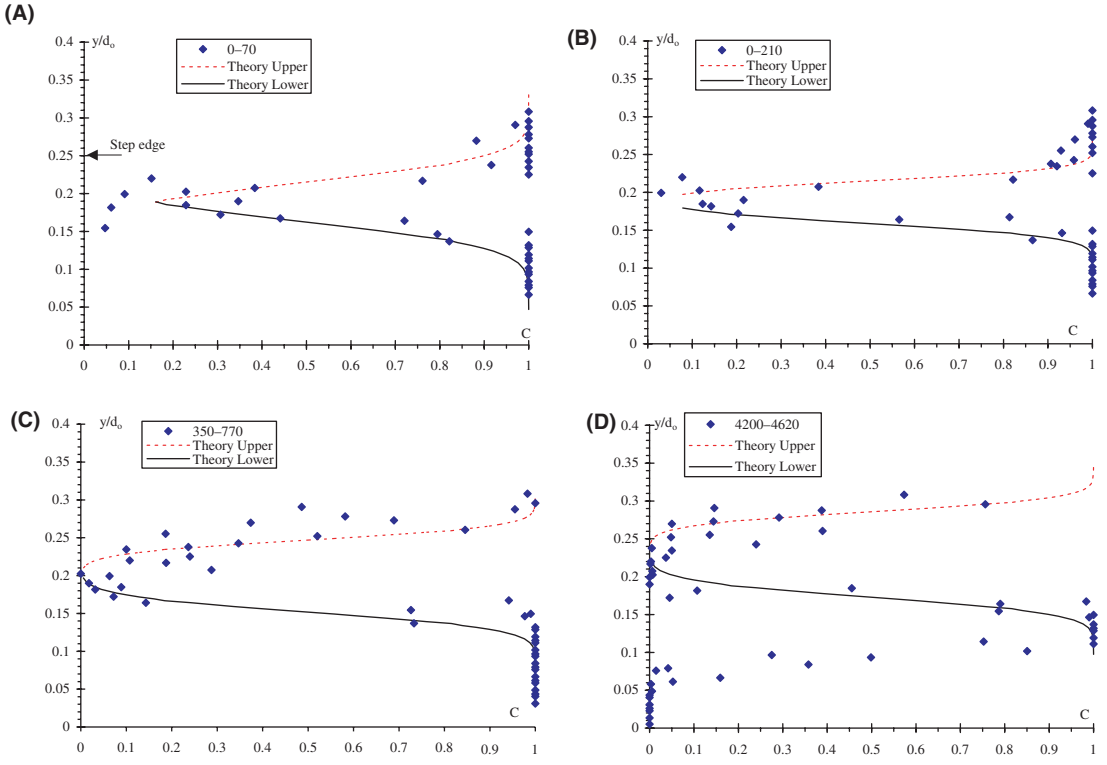

Fig. 3. Dimensionless distributions of instantaneous void fractions in the free-jet flow region ($Q(t = 0+) = 0.070$ m^3/s, $d_0 = 0.283$ m, step 16, $x = 0.1$ m, $V_s = 2.36$ m/s)—comparison with Eqs. (2A) and (2B).

	0–70 mm	0–210 mm	350–770 mm	4200–4620 mm
ΔX (m)	0.07	0.21	0.42	0.42
t (s)	0.015	0.044	0.237	1.87
$t * \sqrt{g/d_0}$	0.087	0.262	1.395	11.0

(A) $t = 0.015$ s, (B) $t = 0.044$ s, (C) $t = 0.237$ s, (D) $t = 1.87$ s—note the start of cavity filling ($y/d_0 < 0.1$).

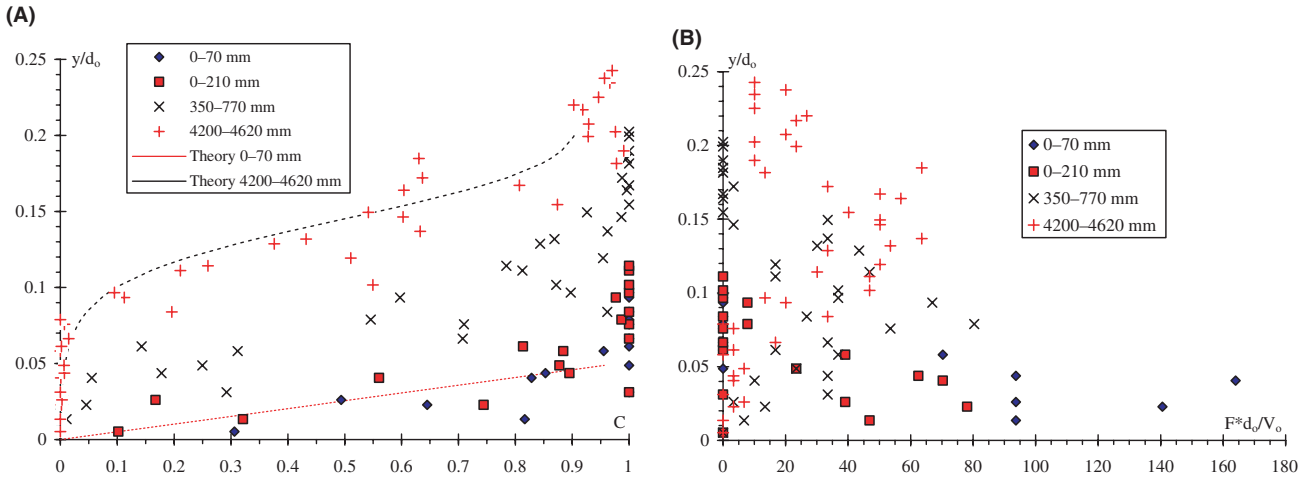

Fig. 4. Dimensionless distributions of instantaneous void fractions and bubble count rates in the impact region ($Q(t = 0+) = 0.070$ m^3/s, $d_0 = 0.283$ m, step 16, $x = 0.3$ m, $V_s = 2.86$ m/s).

	0–70 mm	0–210 mm	350–770 mm	4200–4620 mm
ΔX (m)	0.07	0.21	0.42	0.42
t (s)	0.012	0.037	0.196	1.54
$t * \sqrt{g/d_0}$	0.072	0.215	1.15	9.0

(A) Void fraction distributions—comparison with Eqs. (4) and (5). (B) Bubble count rate distributions.

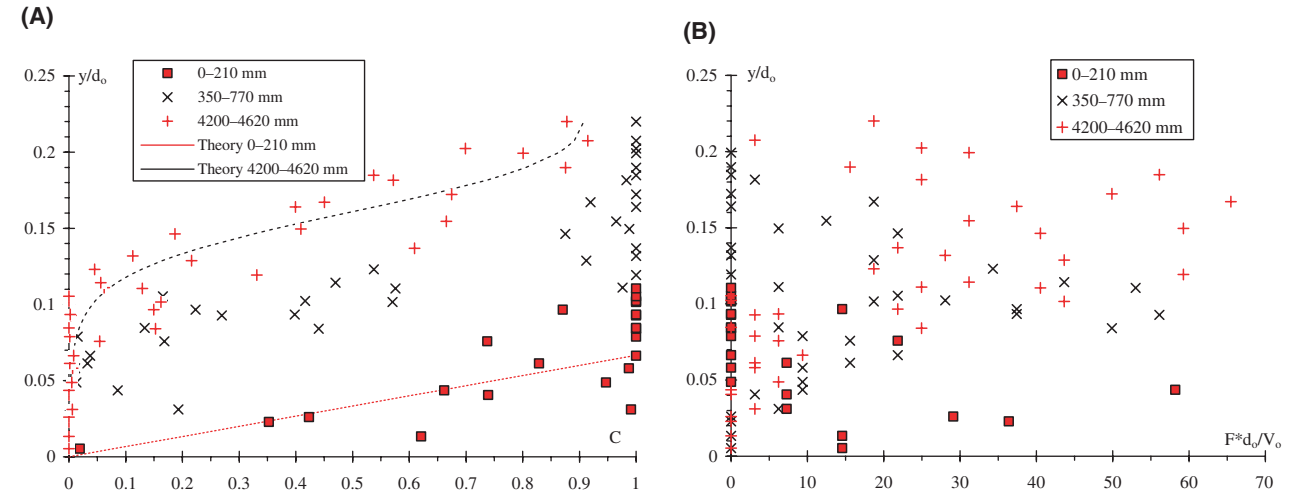

Fig. 5. Dimensionless distributions of instantaneous void fractions and bubble count rates in the horizontal runoff region ($Q(t = 0+) = 0.070$ m^3/s, $d_0 = 0.283$ m, $V_0 = 0.48$ m/s, step 16, $x = 0.8$ m, $V_s = 2.57$ m/s).

	0–210 mm	350–770 mm	4200–4620 mm
ΔX (m)	0.21	0.42	0.42
t (s)	0.040	0.210	1.66
$t * \sqrt{g/d_0}$	0.232	1.23	9.75

(A) Void fraction distributions—comparison with Eqs. (4) and (5). (B) Bubble count rate distributions.

where C is the void fraction, Y_{50} are the characteristic locations where $C = 0.50$ in the nappe, D_t is the air bubble diffusivity, V_s is the surge front celerity, and the function erf is the Gaussian error function:

$$\mathrm{erf}\,(u) = \frac{2}{\sqrt{\pi}} * \int_0^u \exp(-v^2) * \mathrm{d}v \quad (3)$$

Eqs. (2A) and (2B) were developed for the upper and lower nappes of steady water jets, respectively, assuming constant bubble diffusivity [5,3]. They are compared with experimental data in the free-jet region in Fig. 3. In Fig. 3, the diffusivities were deduced from the best data fit, and different values applied to the upper and lower nappes. Overall the results showed an increase in nappe thickness with time at a given location that is consistent with an increase in flow rate as predicted by classical dam break wave theory (e.g. Fig. 3). Note the start of cavity filling for large times t (as illustrated in Fig. 3D). The cavity ultimately became totally filled in steady flow conditions.

In the nappe impact region and in the horizontal runoff, the void fraction distributions at the leading edge of the surging waters had a roughly linear shape:

$$C = 0.9 * \frac{y}{Y_{90}} \quad t * \sqrt{g/d_0} < 1.0 \quad (4)$$

where Y_{90} is the height where $C = 0.90$. For larger times t, the distributions of air concentration exhibited an inverted S-shape that was best described by the diffusion model:

$$C = 1 - \tanh^2\left(K' - \frac{\frac{y}{Y_{90}}}{2 * D_0} + \frac{\left(\frac{y}{Y_{90}} - \frac{1}{3}\right)^3}{3 * D_0}\right) \quad t * \sqrt{g/d_0} > 1.5 \quad (5)$$

where K' and D_0 are functions of the depth-averaged void fraction C_{mean} only [11], and C_{mean} is defined as

$$C_{\mathrm{mean}} = \frac{1}{Y_{90}} * \int_0^{Y_{90}} C * \mathrm{d}y \quad (6)$$

Typical instantaneous void fraction data are presented in Figs. 4A and 5A, in which they are compared with Eqs. (4) and (5).

Figs. 4B and 5B present measured bubble count rate distributions in the nappe impact and horizontal runoff regions, respectively. Overall the data showed consistently large bubble count rates, hence large interfacial areas, at the surge leading edge, while the maximum bubble count rates tended to decrease with increasing time t toward steady flow values.

4.1. Comments

In steady water jet flows, the interfacial aeration at the lower nappe is primarily interfacial aeration induced by high turbulence levels in the mixing layer, while upper nappe aeration is mostly initial aeration (pre-entrainment) of the flow upstream of the step edge [32,10]. In highly unsteady flows, it is believed that the same conclusions are valid. When the shock front takes off at the step edge, the water flow is suddenly subjected to zero pressure difference across the jet and zero bed shear. The lower fluid layers are very rapidly accelerated by momentum redistribution across the jet, while the entire jet flow is gradually accelerated under the influence of the gravity. At the lower nappe, the shear zone is associated with high level of turbulence and strong mixing between air and water. At the upper nappe, the absence of hydrostatic pressure gradient yields zero buoyancy force, associated with a greater ability for air bubbles to be entrained within the water flow.

Eqs. (2A), (2B), (4), (5) are analytical solutions of the advective diffusion of air bubbles developed for steady flow situations. Further, Eqs. (4) and (5) were obtained for uniform equilibrium flows, although they were applied successfully to gradually spatially varied flows (e.g. [10,11]). Such solutions are not strictly applicable to highly unsteady flows, and the relative agreement between these solutions and experimental data is surprising. Note that Eqs. (4) and (5) assume the following distributions of dimensionless turbulent diffusivity of air bubbles:

$$D' = \frac{C * \sqrt{1 - C}}{0.9} \quad t * \sqrt{g/d_0} < 1.0 \quad (7)$$

$$D' = \frac{D_0}{1 - 2 * \left(\frac{y}{Y_{90}} - \frac{1}{3}\right)^2} \quad t * \sqrt{g/d_0} > 1.5 \quad (8)$$

where $D' = D_t/((u_r)_{\mathrm{Hyd}} * \cos\theta * Y_{90})$, D_t is the turbulent diffusivity, $(u_r)_{\mathrm{Hyd}}$ is the bubble rise velocity in hydrostatic pressure gradient and θ is the bed slope. The shape of Eq. (7) is similar to the sediment diffusivity distribution developed by Rouse [27] which yields to the Rouse distribution of suspended matter (e.g. [24,6]).

5. Velocity distributions

In the free-jet region, velocity distributions showed a quasi-uniform profile. This is illustrated in Fig. 6 at one location ($x = 0.2$ m). Despite some scatter, the data suggested overall a reasonably uniform velocity distribution across the nappe thickness. Note some high-speed water projections observed for small times t at $y/d_0 < 0.07$ (Fig. 6, arrow).

Fig. 7 presents typical interfacial velocity distributions in the horizontal runoff region. In Fig. 7A, each data point represents the instantaneous velocity of the first air-to-water interface (i.e. first droplet) detected at each position y. All data were recorded for $t < 0.12$ s. Fig. 7B presents the mean velocity for an entire recording (i.e. for less than 6 s) at each location y. Each data point is the median velocity, or the average velocity if less than ten successful detections occur. In addition,

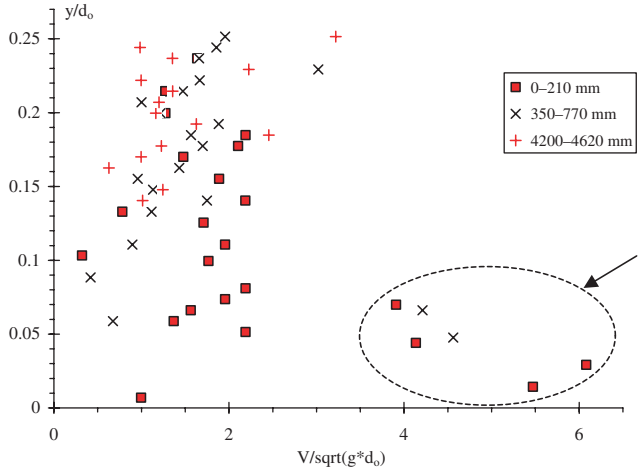

Fig. 6. Dimensionless turbulent velocity distributions in the free-jet region ($Q(t = 0+) = 0.065$ m^3/s, $d_0 = 0.27$ m, step 16, $x = 0.2$ m, $V_s = 2.66$ m/s).

	0–210 mm	350–770 mm	4200–4620 mm
ΔX (m)	0.21	0.42	0.42
t (s)	0.041	0.218	1.72
$t * \sqrt{g/d_0}$	0.25	1.31	10.3

the number of successful interface detections for each location is shown for completeness. Fig. 7C shows the ratio of interfacial velocity standard deviation to mean velocity. For large interface counts, the ratio should tend to the turbulence intensity Tu.

Despite some scatter, experimental data in the horizontal runoff region (incl. Fig. 7A) suggested some boundary layer next to the invert at the surge leading edge. In Fig. 7A, the instantaneous velocity data were compared with an analytical solution of the Navier–Stokes equations (first Stokes problem) for startup flow:

$$\frac{V}{U} = \text{erf}\left(\frac{y}{2 * \sqrt{\nu_T * t}}\right) \quad t * \sqrt{g/d_0} < 0.2 \tag{9}$$

where U is a free-stream velocity, t is the time, and ν_T is the momentum exchange coefficient (Appendix A). Fig. 7B shows that the dimensionless distributions of time-average velocity (over about 5 s.) were quasi-uniform. But the magnitude of the average velocity was consistently smaller than the velocity of the first interface, possibly because of water projections ahead of the surging waters. Fig. 7C highlights high levels of turbulence in the surging flow. In Fig. 7C, the turbulence levels range

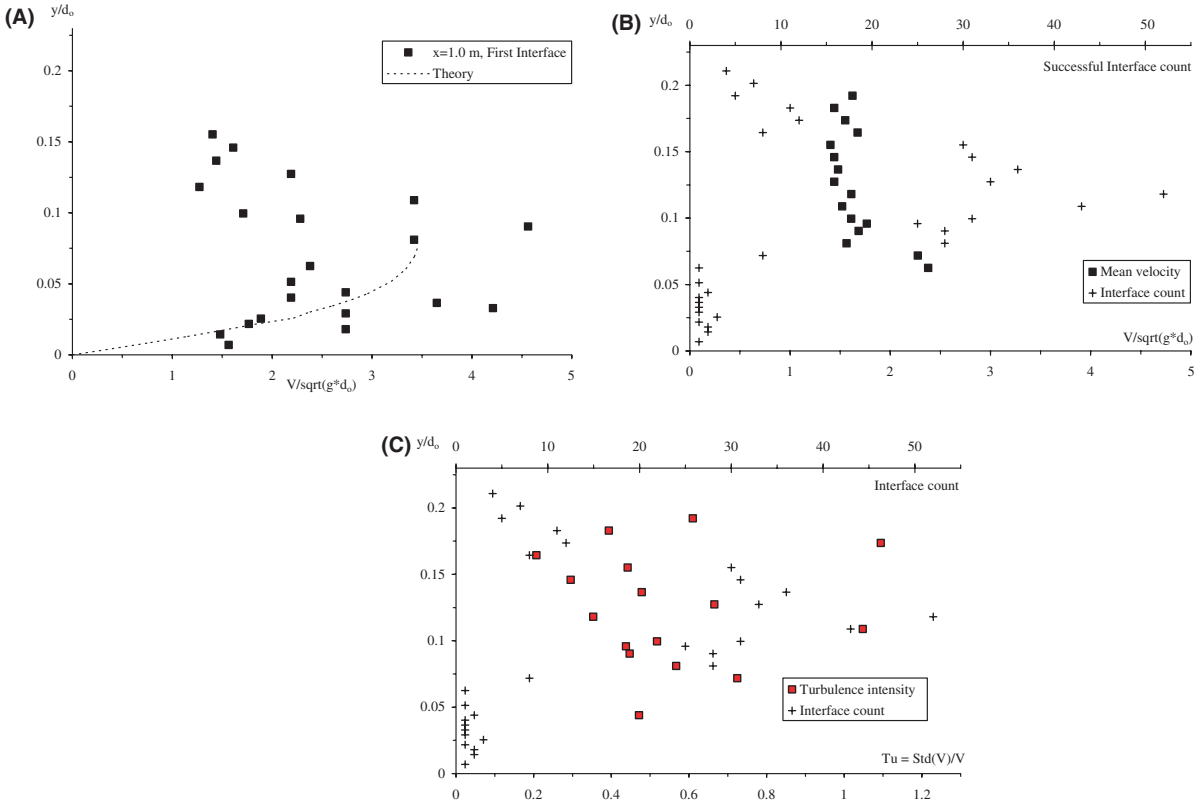

Fig. 7. Dimensionless turbulent velocity distributions at the surge leading edge in the horizontal runoff ($Q(t = 0+) = 0.065$ m^3/s, $d_0 = 0.27$ m, step 16, $x = 1.0$ m). (A) Interfacial velocity of first air-to-water interface ($t < 0.12$ s)—comparison with Eq. (9). (B) Median interfacial velocity (over about 5 s.) and number of successful interface detections. (C) Time-average turbulence intensity (over about 5 s.) and number of successful interface detections.

Table 2
Unsteady boundary layer flow characteristics in the horizontal runoff flow region ($Q(t = 0+) = 0.065$ m^3/s, step 16)

Parameter (1)	$x = 0.6$ m (2)	$x = 0.8$ m (3)	$x = 1.0$ m (4)	Remarks (5)
t (s)	0.0183	0.0183	0.0281	Experimental values
BL thickness (mm)	10–12	15–17	20	Rough experimental estimate
U (m/s)	4.2	6.0	5.7	Best data fit
ν_T (m^2/s)	0.7E−3	1.25E−3	1.2E−3	Best data fit

from 0.2 to 1.1 with a mean value of about 50%. The values were consistent with turbulence levels measured in steady stepped chute flows [25,11,1]. Note, however, that turbulent velocity data were meaningful only for more than 10 successful interface detections (Fig. 7B and C).

5.1. Discussion

In the horizontal runoff flow and next to the invert, the data suggested a boundary layer region in the wave leading edge (e.g. Fig. 7A). The finding is consistent with earlier laboratory experiments [22,16]. The values of U and ν_T (Eq. (9)) were determined from best data fit, and some results are summarised in Table 2. Despite some scatter and crude approximations leading to Eq. (9) (Appendix A), the results implied a turbulent boundary layer.

Based upon present void fraction and velocity measurements in horizontal runoff flow, the air bubble diffusivity D_t and eddy viscosity ν_T which satisfy Eqs. (4) and (9), respectively, yielded a ratio D_t/ν_T of about unity in the surge front. The ratio of bubble diffusivity to eddy viscosity compares the effects of the difference in diffusion of a discrete bubble particle and small coherent fluid structure, as well as the effect of entrained air on the turbulence field. The result (i.e. $D_t/\nu_T \sim 1$) suggest some competition between the air bubble diffusion and momentum exchange processes.

6. Conclusions

New experiments were conducted systematically in surging waters down a 24 m long chute with a succession of abrupt drops. Unsteady air–water flow measurements were performed in the surging waters using arrays of resistivity probes. A new processing technique was developed to analyse the probe outputs yielding quasi-instantaneous air–water flow properties in the free-jet region as well as in the horizontal runoff. The experimental results demonstrated the soundness of the metrology technique.

Visual observations showed that the surging waters propagated at a succession of free jet, immediately downstream of each abrupt drop, nappe impact and horizontal runoff flow. The results showed quantitatively a strong aeration of the surge leading edge. The void fraction distributions followed closely analytical solutions of the air bubble diffusion equation, developed for steady flow conditions. In the horizontal runoff, velocity data suggested the presence of an unsteady turbulent boundary layer next to the invert in the surge front. Overall the results emphasised the complicated nature of the surging flow and its front.

It must be emphasised that present results were focused on a single geometry corresponding to a relatively flat chute, in which the horizontal runoff was a dominant flow motion. On steeper slopes, preliminary observations suggested significantly more complicated unsteady flow processes.

Acknowledgment

The writer thanks his students Chye-guan SIM, and Chee-chong TAN for their help and assistance. He also acknowledges the initial work of Chung-hwee "Jerry" LIM and York-wee TAN.

Appendix I. Analytical solution of the Navier–Stokes equations in surging wave front on a dry bed

In the horizontal runoff, the boundary layer development at the leading edge of the surge is somehow similar to a startup flow. The analytical solution of the Navier–Stokes equations for unsteady plane laminar flows is called the first Stokes problem or Rayleigh problem after Stokes [29] and Rayleigh [26], respectively (e.g. [28, pp. 126–128]). In the start-up flow, the velocity is independent of the x co-ordinate in the flow direction and the continuity equation yields $V_y = 0$. For a laminar flow, the Navier–Stokes equations become:

$$\rho * \frac{\partial V_x}{\partial t} = -\rho * g * \frac{\partial z}{\partial x} - \frac{\partial P}{\partial x} + \mu \frac{\partial^2 V_x}{y^2} \quad \text{(I.1a)}$$

$$0 = -\rho * g * \frac{\partial z}{\partial y} - \frac{\partial P}{\partial y} \quad \text{(I.1b)}$$

where ρ and μ are the fluid density and dynamic viscosity, respectively, z is the vertical elevation and P is the pressure. For a horizontal flow, the gravity force component in the flow direction is zero. The Navier–Stokes equations yield:

$$\frac{\partial V_x}{\partial t} = \nu * \frac{\partial^2 V_x}{\partial y^2} \quad \text{(I.2)}$$

where ν is the kinematic viscosity. Eq. (I.2) is similar to a diffusion equation and a heat conduction equation. Mathematical solutions of diffusion and heat equations have been addressed in two classical references [4,12].

For an advancing surge flow, the boundary conditions are: $V_x = U$ for $y \geqslant 0$ and $t \leqslant 0$, and $V_x(y = 0) = 0$ and $V_x(y \to +\infty) = U$ for $t > 0$. The analytical solution of Eq. (I.2) is

$$\frac{V_x}{U} = \text{erf}\left(\frac{y}{2 * \sqrt{\nu * t}}\right) \quad \text{(I.3)}$$

where y is the distance normal to the invert and the function erf is the Gaussian error function defined as

$$\text{erf}(u) = \frac{2}{\sqrt{\pi}} * \int_0^u \exp(-\tau^2) * d\tau \quad \text{(I.4)}$$

The reasoning may be extended to unsteady turbulent boundary layer flow with constant momentum exchange coefficient (or "eddy viscosity") ν_T. The analytical solution of the Navier–Stokes equations becomes:

$$\frac{V_x}{U} = \text{erf}\left(\frac{y}{2 * \sqrt{\nu_T * t}}\right) \quad \text{(I.5)}$$

References

[1] A. Amador, M. Sanchez-Juny, J. Dolz, F. Sanchez-Tembleque, J. Puertas, Velocity and pressure field in skimming flow in stepped spillways, in: Proc. Intl. Conf. on Hydraulics of Dams and River Structures, Balkema Publ., Tehran, Iran, The Netherlands, 2004, p. 8.

[2] A. Bornschein, R. Pohl, Dam break during the flood in Saxon/Germany in August 2002, in: J. Ganoulis, P. Prinos (Eds.), Proc. 30th IAHR Biennial Congress, Thessaloniki, Greece, vol. C2, 2003, pp. 229–236.

[3] T. Brattberg, H. Chanson, L. Toombes, Experimental investigations of free-surface aeration in the developing flow of two-dimensional water jets, J. Fluids Eng., Trans. ASME 120 (4) (1998) 738–744.

[4] H.S. Carslaw, J.C. Jaeger, Conduction of Heat in Solids, second ed., Oxford University Press, London, UK, 1959, 510 p.

[5] H. Chanson, Study of air entrainment and aeration devices, J. Hydraul. Res., IAHR 27 (3) (1989) 301–319.

[6] H. Chanson, The Hydraulics of Open Channel Flows: An Introduction, Butterworth–Heinemann, Oxford, UK, 1999, 512 p.

[7] H. Chanson, The Hydraulics of Stepped Chutes and Spillways, Balkema, Lisse, The Netherlands, 2001, 418 p.

[8] H. Chanson, Sudden flood release down a stepped cascade, unsteady air–water flow measurements, applications to wave run-up, flash flood and dam break wave, Report CH51/03, Department of Civil Engineering, University of Queensland, Brisbane, Australia, 2003, 142 p.

[9] H. Chanson, Experimental study of flash flood surges down a rough sloping channel, Water Resour. Res. 40 (3) (2004) 12, paper W03301, Ref. 10.1029/2003WR002662.

[10] H. Chanson, L. Toombes, Energy dissipation and air entrainment in a stepped storm waterway: An experimental study, J. Irrig. Drain. Eng., ASCE 128 (5) (2002) 305–315.

[11] H. Chanson, L. Toombes, Air–water flows down stepped chutes: Turbulence and flow structure observations, Int. J. Multiphase Flow 28 (11) (2002) 1737–1761.

[12] J. Crank, The Mathematics of Diffusion, Oxford University Press, London, UK, 1956.

[13] T.R.H. Davies, Debris flow surges—a laboratory investigation, Mitteilungen Der Versuchsanstalt Fur Wasserbau, Hydrologie Und Glaziologie, vol. 96, ETH-Zurich, Switzerland, 1988, 122 p.

[14] R. Dressler, Comparison of theories and experiments for the hydraulic dam-break wave, in: Proc. Intl Assoc. of Scientific Hydrology Assemblée Générale, Rome, Italy, vol. 3, no. 38, 1954, pp. 319–328.

[15] L. Escande, J. Nougaro, L. Castex, H. Barthet, Influence de Quelques Paramètres sur une Onde de Crue Subite à l'Aval d'un Barrage ('The Influence of certain Parameters on a Sudden Flood Wave Downstream from a Dam.'), Jl La Houille Blanche 5 (1961) 565–575 (in French).

[16] K. Fujima, N. Shuto, Formulation of frictions laws for long waves on a smooth dry bed, Coast. Eng. Jpn. 33 (1) (1990) 25–47.

[17] F.M. Henderson, Open Channel Flow, MacMillan Company, New York, USA, 1966.

[18] A. Hoque, Air bubble entrainment by breaking waves and associated energy dissipation, Ph.D. thesis, Department of Architecture and Civil Engineering, Toyohashi University of Technology, Japan, 2002, 151 p.

[19] B. Hunt, Asymptotic solution for dam-break problems, J. Hydr. Div., Proc., ASCE 108 (HY1) (1982) 115–126.

[20] H.H. Hwung, J.M. Chyan, Y.C. Chung, Energy dissipation and air bubbles mixing inside surf zone, in: Proc. 23rd Intl Conf. on Coastal Eng., vol. 1, ASCE, Venice, Italy, 1992, pp. 308–321 (Chapter 22).

[21] A. Jensen, G.K. Pedersen, D.J. Wood, An experimental study of wave run-up on a steep beach, J. Fluid Mech. 486 (2003) 166–188.

[22] A. Mano, Boundary layer developed near surging front, Coast. Eng. Jpn. 37 (1) (1994) 23–39.

[23] J.S. Montes, Hydraulics of Open Channel Flow, ASCE Press, New York, USA, 1998, 697 p.

[24] P. Nielsen, Coastal bottom boundary layers and sediment transport, Advanced Series on Ocean Engineering, vol. 4, World Scientific Publ., Singapore, 1992.

[25] I. Ohtsu, Y. Yasuda, Characteristics of flow conditions on stepped channels, in: Proc. 27th IAHR Biennal Congress, San Francisco, USA, Theme D, 1997, pp. 583–588.

[26] L. Rayleigh, On the motion of solid bodies through viscous liquids, Philos. Mag. 21 (1911) 697–711.

[27] H. Rouse, Modern conceptions of the mechanics of turbulence, Trans., ASCE 102 (1937) 463–543.

[28] H. Schlichting, K. Gersten, Boundary Layer Theory, eighth ed., Springer Verlag, Berlin, Germany, 2000, 707 p.

[29] G.G. Stokes, On the effect of internal friction of fluids on the motion of pendulums, Trans. Camb. Philos. Soc. 9 (Part II) (1856) 8–106.

[30] B. Stutz, J.L. Reboud, Experiments in unsteady cavitation, Exp. Fluids 22 (1997) 191–198.

[31] B. Stutz, J.L. Reboud, Measurements within unsteady cavitation, Exp. Fluids 29 (2000) 545–552.

[32] L. Toombes, Experimental study of air–water flow properties on low-gradient stepped cascades, Ph.D. thesis, Department of Civil Engineering, The University of Queensland, 2002.

[33] Z.Y. Wang, Initiation and mechanism of two phase debris flow, in: WU et al. (Eds.), Proc. Conf. on Flood Defence'2002, Science Press, 1648, 2002, p. 1637.

[34] M.J.A. Walkden, Model wave impulse loads on caisson breakwaters: Aeration, scale and structural response, Ph.D. thesis, University of Plymouth, UK, 1999, 250 p.

[35] D.J. Wood, G.K. Pedersen, A. Jensen, Modelling of run-up of steep non-breaking waves, Ocean Eng. 30 (2003) 625–644.